Universität zu Köln

II. Physikalisches Institut

Bachelorarbeit

Raman spectroscopy on the topological insulator $BiSbTeSe_2$

Philipp Stein
Matrikelnummer: 5411637

Erstkorrektor: Prof. Paul H. M. van Loosdrecht
Zweitkorrektor: Prof. Alexander Grüneis

Köln, 7.10.2015

Contents

1 Motivation

The research field of topological insulators is currently one of the most interesting developments in solid state physics. In the years after the effect was experimentally verified in 2007 [1], more and more topological insulators were discovered and the discovery is still going on. Investigating the properties of a topological insulator is thus of multiple use. It gives insight into an important application of the electronic band model, which is considerable, since the model itself has been well known in science for a long time, and forms a conclusion and generalization for other current research topics like the Quantum-Spin-Hall-Effect. The topological insulator investigated in this thesis is $BiSbTeSe_2$, abbreviated BSTS. It was found to show a very interesting temperature dependence of bulk charge carriers, which has a minimum at about T = 50K. [2] Further measurements on BSTS may potentially lead to the discovery of other unexpected temperature-dependent effects. Raman spectroscopy is an easy way of analysing the temperature-dependant phonon behaviour of a material, which may lead to the discovery of a similar temperature-induced effect and provide information about electron-phonon coupling in BSTS. Since this is also one of the first measurements done with the newly installed Macro Raman setup, special attention will be given to the quality of the Raman spectra.

2 Theory

2.1 Topological Insulators

Topological insulators can be called a generalization of the Quantum-Spin-Hall effect (which is a two-dimensional effect) in three dimensions [3,4]. In principle, they are insulating in the bulk, but conductive on the surface. This property makes them interesting for new applications in fields like information technology.

In the bulk, the electronic band strcuture resembles that of an ordinary insulator [5]. The valence and conduction band are separated by an energy gap, which in case of $BiSbTeSe_2$ (BSTS) is about 0.17 eV wide [6]. The Fermi level ideally lies in this gap. If it doesn't, it can be moved there by compensation doping. Near the boundaries of the material, the surface potential has to be included in the Dirac equation for the Landau levels. This leads to the levels being bent upwards near the surface, an effect that is illustrated in Fig. 1.

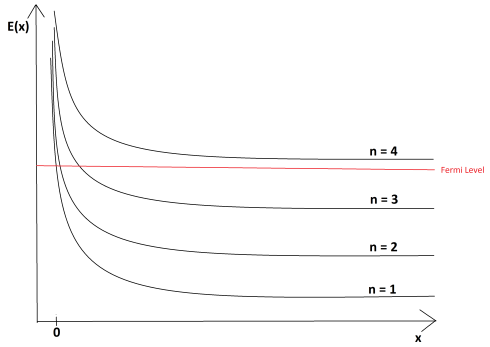

Figure 1: Illustration of the up-bending of Landau levels caused by the surface potential (in two dimensions). x marks the depth in the probe

As can be seen in the image, this leads to intersections between the Landau levels and the Fermi level and therefore to the creation of surface states. For the following considerations, it should be noted that topological insulators ideally show a strict time-reversal symmetry. According to the Kramers theorem, all Eigenstates of a time-reversal invariant Hamiltonian are degen-

erate. In this case, each surface state consists of one spin-up state and one spin-down state with opposing momenta ±k [7]. The charge carriers are not evenly distributed in k space, as it would be the case for normal conduction. Instead, their spin is always locked at a right angle to their momentum, an effect that is called spin-momentum locking [5]. The coupling of the spins to the momentum also results in a coupling of the different spins to an opposing direction of movement. This leads to a separation of spin up and spin down carriers. They will eventually accumulate on the edges of the material. It should be recognized at this point, that this process and especially the creation of spin current bears great resemblance to the Spin-Hall-Effect, as mentioned before. The time-reversal symmetry protects the surface states of a topological insulator against time-reversal-symmetric perturbations. However, magnetic perturbations are able to destroy the conductive surface states [8]. This vulnerability is the reason why topological insulators can not be seen as an example of topologically ordered states [9]. An ideal depiction of the electronic band structure including surface states is shown in Fig. 2.

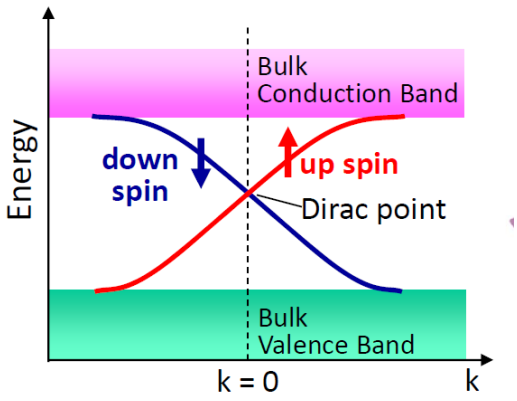

Figure 2: Band structure of an ideal topological insulator. The surface states are split up in spin up and spin down states and form a Dirac cone between valence and conduction band [10].

For BSTS, the Fermi level crosses the Dirac point [2]. Also, contrary to the image in Fig. 2, [2] suggests that there are "puddles" of charge carriers in the bulk in BSTS, which deform the valence and conduction band. Most topological insulators have band structures that deviate from this ideal pic-

ture. As an example, the band structures for Bi_2Se_3 and Bi_2Te_3 are displayed in Fig. 3.

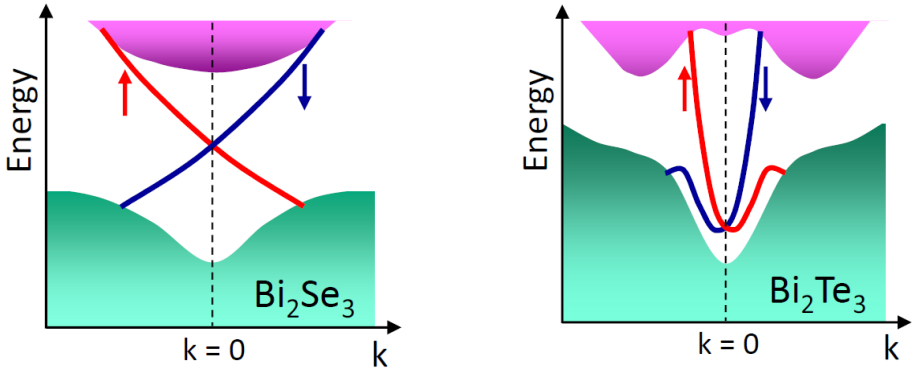

(a) (b)

Figure 3: Band structures for (a) Bi_2Se_3 and (b) Bi_2Te_3 [10].

The conductivity of these surface states is exceptionally high because practically no dissipation occurs [11]. For the moving electrons, scattering could be a way to lower conductivity. But for a fixed energy of the carriers, all other state with the same spin orientation have the same momentum and thus, the conductivity would not change. Scattering into the opposite spin orientation states is prohibited, because this would break the time-reversal symmetry, which is not allowed here. Because of this, backscattering is highly suppressed in the conduction channels [7].

2.2 Raman Scattering

The experimental method used here to examine the topological insulator is Raman spectroscopy. It was discovered by C.V. Raman and K.S. Krishnan in 1928 [12]. The following section will provide a classical approach to the process of Raman scattering following the one given in [13]. Additionally, it will illustrate how it can be used to investigate solids.

In an atomic or molecular lattice, every possible lattice vibration can be described as a superposition of a limited number of normal modes. Following the quantum mechanical wave-particle duality, in solid state physics,

these normal modes are usually described as quasiparticles which are called phonons.

When light falls onto a solid, its electric field E can interact with its electronic states. The field can be written as

$$E(t) = A \cdot e^{-i\omega_E t} + c.c.$$

This electric field interacts with the electrons in the material, causing them to oscillate and creating a dipole moment $\mu(t)$ which is proportional to E(t):

$$\mu(t) = \alpha \cdot E(t)$$

α is called the polarizability. Since the nuclei of the atoms also consist of charged particles, they are influenced by the electric field, too. However, the frequency of the electric field is so high that the heavy nuclear particles can't follow the oscillation, thus minimizing the interaction between nuclear particles and incoming light. Nonetheless, as the electronic potential depends on the position of the nucleus, it plays an important role. This connection results in the dependency of the polarizability on the nuclear coordinate q. Since this dependency can be assumed to be small, it can be approximated by a Taylor series in q:

$$\alpha(t) = \alpha_0 + \frac{\delta\alpha}{\delta q} * q(t) + O(q^2)$$

If we assume that the nuclear motion, which is a phonon mode in the lattice of the sample, is a harmonic oscillation with $\mathrm{Q(t)} = \mathrm{Q_0[e^{i\omega_q t} + e^{-i\omega_q t}]}$, the electric dipole moment can be written as

$$\mu(t) = \alpha_0 A e^{-i\omega_E t} + A\frac{\delta\alpha}{\delta q}[e^{-i(\omega_E - \omega_q)t + i\phi} + e^{-i(\omega_E + \omega_q)t + i\phi}] + c.c.$$

The equation states that the dipole moment of the electrons and therefore the radiation that is emitted by the electrons' movement can oscillate at three different frequencies. In the first case, the dipole moment oscillates

at the frequency ω_E, which is the frequency of the incoming light. The system is excited to a virtual energy level and immediately falls back down to the electronic ground state. Since the frequency and therefore the energy of the photons has not changed, this is called elastic scattering or Rayleigh scattering. The second term of the equation describes dipole oscillations at the shifted frequencies $\omega_E - \omega_q$ and $\omega_E + \omega_q$. The first term corresponds to the excitation of the system to an electronic state with the energy $\mathrm{E_a}$, the creation of a phonon at that energy and the emission of light with the lowered energy $E - E_a$. This process is called Stokes scattering. Similarly, the incoming photon may return the the system from an excited electronic state at energy E_a to a the electronic ground state under excitation of a photon with the energy $E + E_a$. This process corresponds to the second term in the equation above. Physically, it goes along with the annihilation of a phonon and is called Anti-Stokes scattering. As the energy of the incoming and outgoing photon are not the same, both Stokes and Anti-Stokes scattering can be understood as an inelastic photon-phonon interaction. The cross sections for both interactions are dependant on the material, but generally, the fraction of Rayleigh and Raman scattering cross sections can be estimated as [14]

$$\frac{\sigma_{Rayleigh}}{\sigma_{Raman}} \approx 10^8$$

The three processes are displayed in Fig. 4.

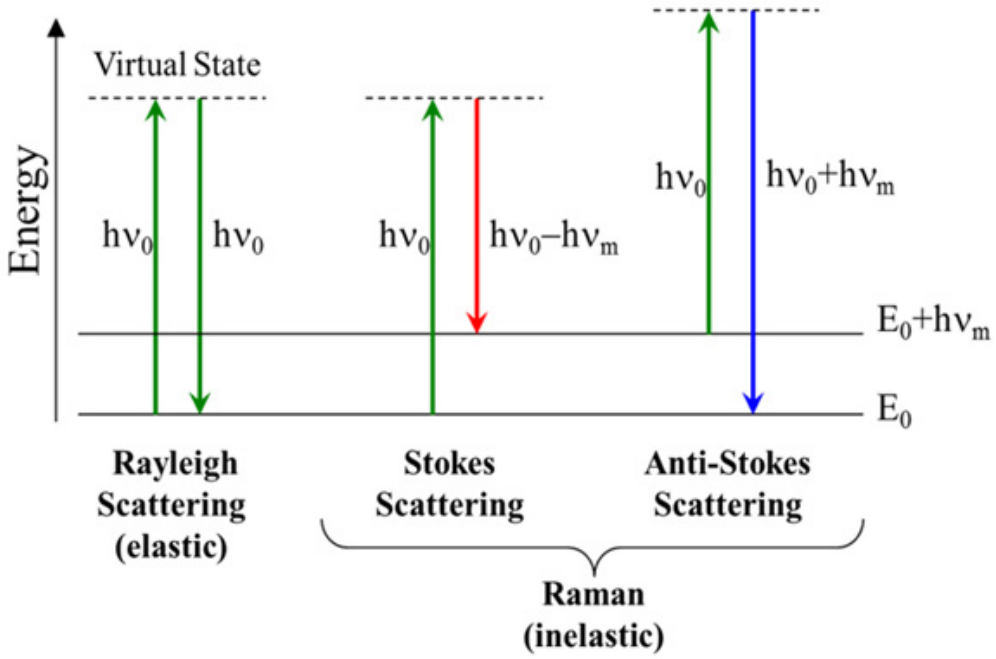

Figure 4: Illustration of the three possible light scattering processes in solids

Since the excited phonon states are each corresponding to a lattice vibration of the investigated solid, a spectroscopic analysis of the scattered light can give detailed information about its phononic behaviour.

Another important consequence of the equation calculated before is that for $\frac{\delta\alpha}{\delta \mathrm{q}} = 0$, only photons with $\omega = \omega_{\mathrm{E}}$ will be emitted. This leads to an important selection rule for Raman scattering: It can only occur if $\frac{\delta\alpha}{\delta \mathrm{q}} \neq 0$, meaning that the polarizability needs to change for the Raman process. Hence, a mode that complies with this condition is called Raman active. Further electrodynamic calculations lead to an equation for the intensity of Raman scattered light [15].

$$I_{Raman} \propto \left| \vec{e_I} \left(\frac{\delta\alpha}{\delta q} \right)^2 \vec{e_{II}} \right|$$

$\vec{e_I}$ and $\vec{e_{II}}$ are the unit vectors of the incoming light and the reflected light, respectively. Since the polarizability is not constant in all directions, it has to be written as α_{ij}, which is a tensor of the second order and is characteristic

for a specific mode. This tensor is called the Raman tensor. The Raman tensors for all possible modes m can be combined in one Raman tensor of the third order, which then fully describes the Raman related properties and behaviour of the examined solid.

$$R = \left(\frac{\delta\alpha_{ij}}{\delta q_m}\right)$$

2.2.1 Modes and Selection Rules

Besides Raman spectroscopy, infrared spectroscopy provides another possibility for spectroscopic analysis of phonon modes in solids. In infrared spectroscopy, the intensity of the scattered light is given as [14]

$$I_{IR} \propto \left|\left(\frac{\delta\mu}{\delta q}\right)\right|^2$$

In topological insulators, the inversion symmetry leads to the rule of mutual exclusion between Raman activity and infrared activity [14]. The condition for Raman activity is $\frac{\delta\alpha}{\delta q} \neq 0$ and the condition for infrared activity is $\frac{\delta\mu}{\delta q} \neq 0$, which for systems with inversion symmetry is equivalent to $\frac{\delta\alpha}{\delta q} = 0$.

Generally, the phonon modes of any solid can be visualized using dispersion curves. A very simple example can be seen in Fig. 5.

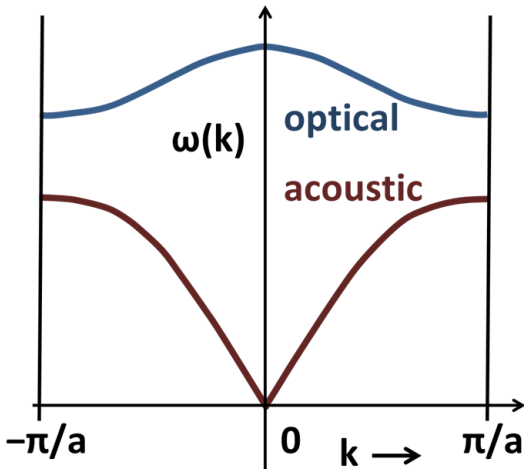

Figure 5: Dispersion curves of a linear diatomic chain in the first Brillouin zone

Each of the branches in such a dispersion diagram corresponds to one phonon mode. On the basis of these curves, we can distinguish between modes with $w \approx 0$ for $k \to 0$, which are called acoustic modes, and modes with $w \neq 0$ for $k \to 0$, which are called optical modes. In a solid, the total number of modes depends on the number of atoms in the unit cell. There are always three acoustical and $3N - 3$ optical modes. Raman spectroscopy uses lasers with wavelengths that correspond to visible or infrared light, usually in the range between 400 nm and 700 nm. Since the diameter of the Brillouin zone in a common crystal lattice is at usually about $10^{-10}\mathrm{cm}^{-1}$, in Raman spectroscopy, modes can only be probed near the center of the Brillouin zone, which is called the Γ-point. To probe at different wavenumbers, other research methods like neutron scattering have to be used. As mentioned above, the frequency and therefore the energy of acoustic phonons vanishes at the Γ-points. Thus, only optical phonons can be measured using Raman spectroscopy. For measuring acoustic phonons, Brillouin scattering can be used.

Raman active modes can be further classified by symmetry properties, first of all by energy degeneration. Doubly degenerate modes are labelled as E modes, triply degenerate modes would as F modes (or T modes), and quadruply and quintuply degenerate modes as G and H modes, respectively. Non-degenerate modes can be further classified by their symmetry. Modes that are symmetric with respect to the principal rotational axis $\mathrm{C_n}$ are called A modes, otherwise it would be B modes. As mentioned before, modes have to be symmetric with respect to the center of inversion in order to be Raman active. This is indicated by the subscripts g (*gerade*). Non-symmetric and therefore infrared active modes would get the subscript u (*ungerade*). Additionally, the subscripts 1 is used to indicate symmetry with respect to the $\mathrm{C_2}$ axis perpendicular to the $\mathrm{C_n}$ axis.

3 Experimental

3.1 Setup

In this section, I want to focus on the optical setup which was built to measure and analyse the Raman scattered light. It is sketched out in Fig. 6.

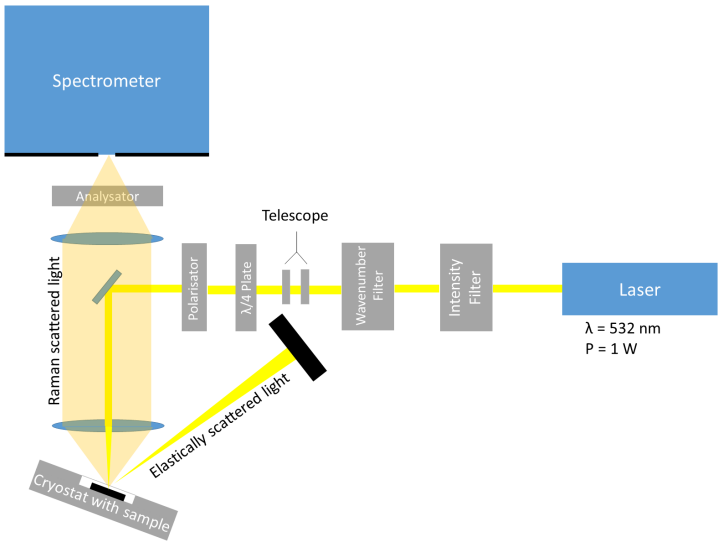

Figure 6: Sketch of the Raman setup

Since the macro optical part of the setup was installed right before the presented measurements and was essentially tested by it, a detailed description of its components will be given here.

The laser used for this experiment is a Cobolt laser that emits light with a wavelength of 532 nm and power up to 1 W.

The sample is mounted in a cryostat, which can be hermetically sealed. It has contacts for a vacuum pump, for helium supply and for a temperature controller. Using the vacuum pump, the pressure inside the cryostat can be lowered to about 10^{-6} mbar. The temperature controller measures the temperature near the sample and has a built-in heater which can be controlled manually or automatically by setting a target temperature. The helium flux has to be controlled manually.

The laser beam passes an intensity filter and a wavelength filter. The wavelength filter, which can also be called interference filter, is needed to suppress the emission of light at wavelengths that deviate from 532 nm. The intensity filter is used to control the power of the laser beam. To control the the polarisation, a polarisator is installed. A polarised excitation is needed so that the measured peaks can be attributed to specific modes of the investigated solid later, as the direction of polarisation gives information about a mode's Raman tensor. There are two possibilities of setting the polarisation. It can be set parallel to the detector's entrance slit, leading to parallel polarization, or rotated by 90°, which is called cross polarized. A $\lambda/4$ plate is put in front of the polarisator. It makes the light circularly polarised, which makes sure that a polarisation change using the polarisator does not result in an intensity change. Using a tiny mirror, the light is directed into an objective which focusses the beam onto the sample inside the cryostat. The mirror can be moved to adjust the light to the optical axis of the spectrometer. The cryostat is tilted so that the elastically scattered light from the sample does not get back into the objective. The Raman scattered light, however, gets back into the objective. It is then focussed by a lens with a focal length of f = 30 cm onto the entrance slit of the spectrometer. In front of the slit, an analysator filters the polarization. A vital part of the experiment is the process of focussing the light on the sample. In many Raman setups, this is done using a microscope. Such a setup is then called micro Raman. For this experiment, no microscope is used. Instead, the focussing can be done by adjusting the distance of the objective, which is mounted on a translation stage. By moving the cryostat, which is mounted on an x-y-stage, the position of the laser spot on the sample can be moved. It is important to find a position where the reflectivity is low in order to minimize Rayleigh scattered light entering the spectrometer. Because this focussing process and the whole setup in general only consists of large-scaled parts, this is called macro Raman. There are a few advantages and disadvantages to this method. The disadvantage of a microscope is that the croystat can not be tilted and thus, only backscattering configurations are possible. This makes it difficult to suppress Rayleigh scattered light. Additional to the Raman signal from the

sample, the air that the laser beam passes though on its path also generates a Raman spectrum which is also measured in micro Raman setups. On the other hand, a microscope causes a smaller laser spot and better focus on the sample. A micro Raman setup can be used to probe specific areas in a material. This is useful for the detailed analysis of inhomogeneous samples. For some samples, the small laser spot can lead to the micro-optical setup damaging the sample because of the increased power density.

The Raman signal is further processed by a Horiba Jobin Yvon T64000 spectrometer. A sketch of the spectrometer can be found in Fig. 7.

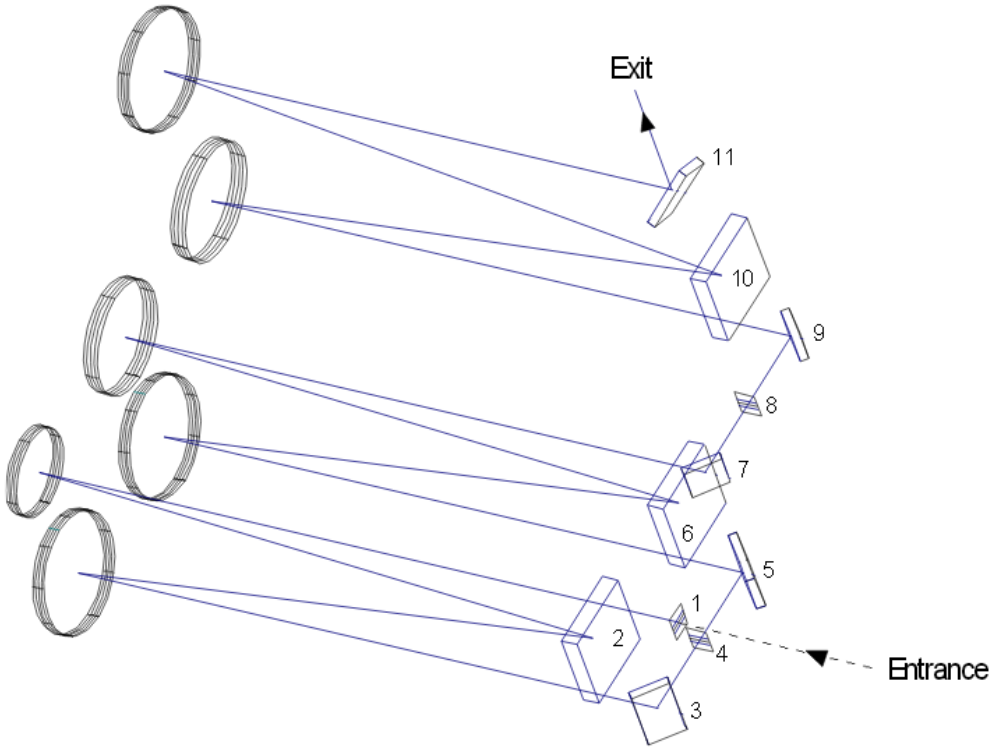

Figure 7: Sketch of the Horiba Jobin Yvon T64000 spectrometer [16]

According to [16], the spectrometer consists of the entrance slit (0-2mm, No. 1 in the picture), two manual intermediate slits (0-50mm, No. 4 and 0-25mm, No. 8), and mainly three aberration corrected holographic gratings at 1800 $\frac{\text{gr}}{\text{mm}}$ (No. 2, 6 and 10). It can be used in double additive adaptation or

subtractive adaptation, in our case, the subtractive mode is used. The light is finally analysed by a CCD camera and the intensity of Stokes scattered light is determined in dependence of the energy shift.

3.2 The Material: $BiSbTeSe_2$

$BiSbTeSe_2$ belongs to the R-3m hexagonal space group [6]. It has a quintuple layer structure. The five layers that form the quintuples are covalently bound, while the quintuples are only weakly bound by van-der-Waals forces [17]. The layers are arranged in the pattern VI(1) - V - VI(2) - V - VI(1). V and VI stand for the group of the elements in the periodic system, so V can be Bismuth or Selenium and VI can be Tellerium or Antimony. The VI(2) plane is also a center of inversion. [18] The crystal structure is shown in Fig. 8.

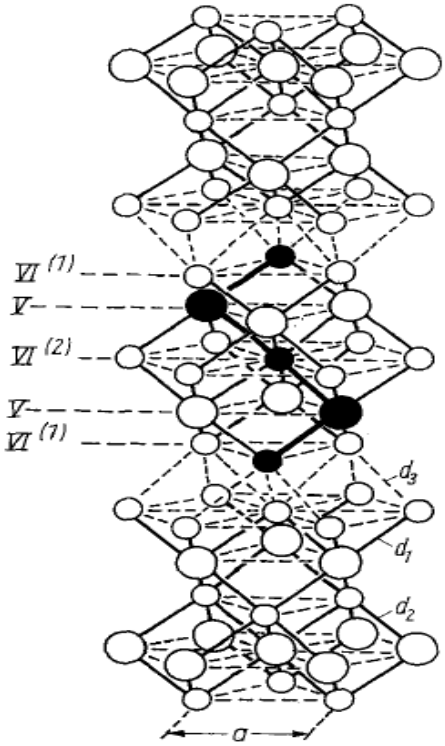

Figure 8: Quintuple layer structure of the R-3m hexagonal space group [18].

In case of BSTS, the VI(1) plane shown in the picture consists of Selenium

and Tellurium atoms, the V plane consists of Bismuth and Antimony atoms and the VI(2) is a pure selenium plane. [10] Since the primitive unit cell contains five atoms, BSTS has 15 modes, which divide into three acoustical modes and 12 optical modes. According to group theory, the optical modes are classified into $2A_{1g}$, $2E_g$, $2A_{1u}$ $2E_u$. The A_{1u} and E_u modes are infrared active and were successfully observed in [2]. The A_{1g} and E_g modes are Raman active, so they are expected to appear in the Raman spectrum for BSTS. The Raman tensors according to [18,19] are:

$$A_{1g}: \begin{pmatrix} a & 0 & 0 \\ 0 & a & 0 \\ 0 & 0 & b \end{pmatrix}, E_g^1: \begin{pmatrix} c & 0 & 0 \\ 0 & -c & d \\ 0 & d & 0 \end{pmatrix}, E_g^2: \begin{pmatrix} 0 & -c & -d \\ -c & 0 & 0 \\ -d & 0 & 0 \end{pmatrix}$$

The displacements corresponding to the normal modes are shown in Fig. 9.

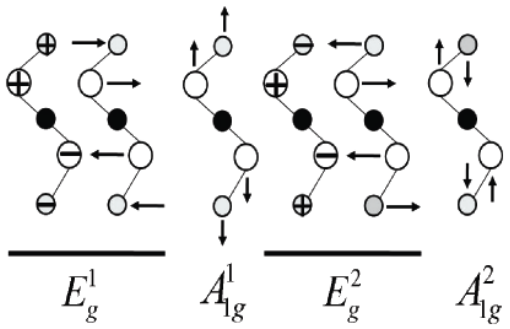

Figure 9: Depiction of the four Raman active normal modes [20]

The sample of $BiSbTeSe_2$ that was used for the measurements has a square-shaped surface with an edge length of about 2 mm and is about 1 mm thick.

3.3 Measurement

As preparation for our measurement, the sample was prepared by cleaving along the trigonal axis using adhesive tape. It was placed inside a cryostat which is installed in the setup as previously described.

The laser power is set to 400 mW and the resulting power near the sample is measured. It can be controlled by using the intensity filter that was described previously. To suppress thermal noise, the spectrometer's CCD camera is cooled down to a temperature of $-133°$C using liquid nitrogen.

For the first series of measurements, the polarisator was set parallel to the entrance slit. The width of the first internal slit was set to 26725 μm and the central spectrometer position was adjusted to 335 cm^{-1}. It should be noted that for this measurement, the analysator described in the *Setup* section was not yet installed. The pressure in the cryostat was lowered to $5 \cdot 10^{-7}$ mbar and the sample was cooled down to a temperature of 280K. The laser power was 14 mW right in front of the sample. The exposure time for one measurement was set to 5 minutes and ten measurements were done for the temperatures 280K, 200K, 150K, 100K, 90K, 80K, 70K, 60K, 50K, 40K, 30K and 6K. These temperatures were chosen because as mentioned in the *Motivation* section, the temperature range around T = 50K should be especially worth researching. During the measurement at T = 150K, the intensity of the Raman scattered light considerably decreased, which resulted in a low signal-to-noise ratio. So the laser spot was moved to a position where the reflectivity of the sample was visibly higher. A second series of measurements was done about a month later with the polarisator rotated 90° in comparison to the first series. The central spectrometer position was moved to 320 cm^{-1} and the power of the laser beam near the sample was 10 mW. The exposure time for a single measurement was set to seven minutes here. Measurements were done for the temperatures 6K, 30K, 55K, 100K, 40K, 50K, 60K, 80K and 20K (in the listed order). Similar to the previous measurement, before the measurement at T = 20K, the laser spot had to be changed, this time because of a strong Rayleigh signal. A comparison of the obtained signals before and after changing the spot on the sample can be seen in Fig. 10.

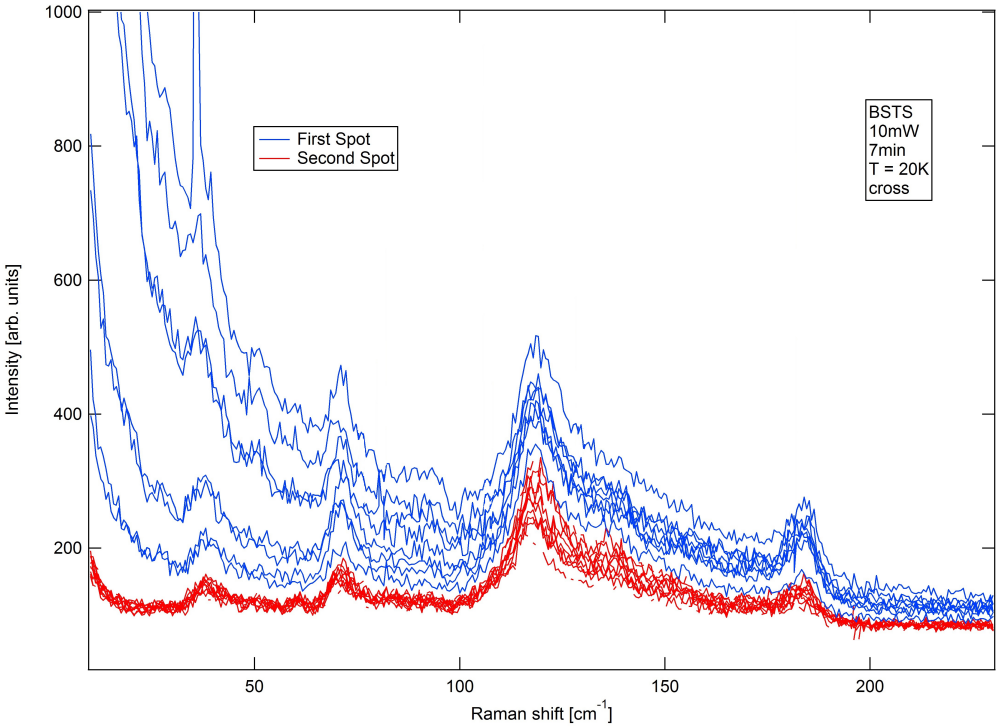

Figure 10: Comparison of the Raman spectra of BSTS before (blue) and after (red) changing the laser spot on the sample

This should be kept in mind for later analysis.

4 Results and Discussion

4.1 The Low Temperature Spectra

Prior to discussing the graphs, the single spectra are added up so that we get only one overall spectrum for each temperature, and the so called spikes, which are peaks caused by cosmic radiation and can be seen in Fig. 11, are removed.

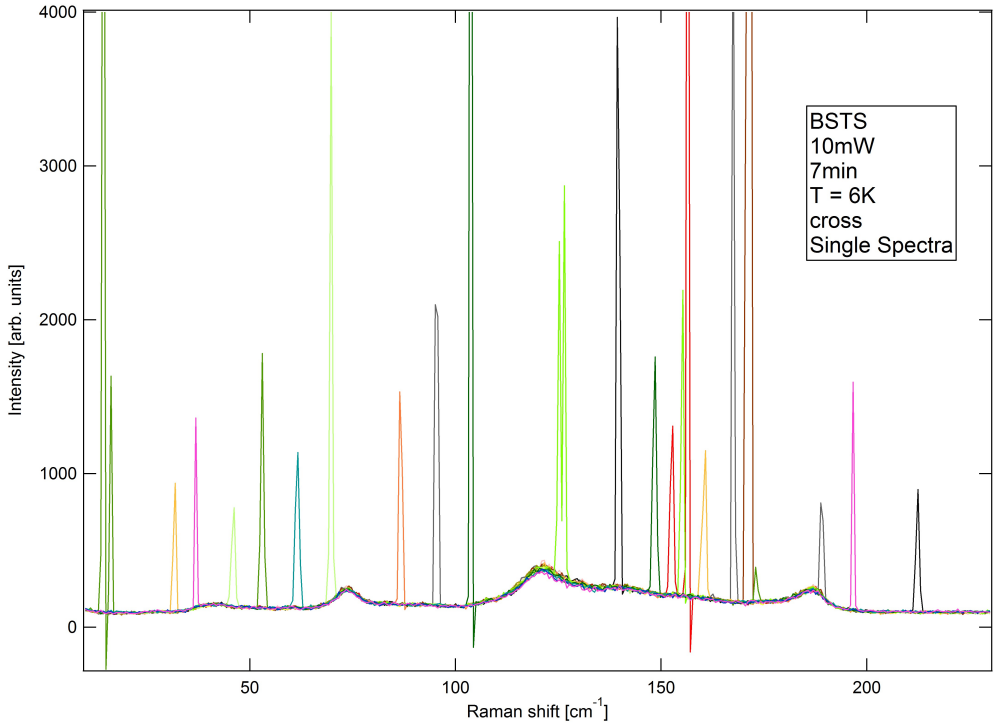

Figure 11: Raw data from single measurements on BSTS at T = 6K with cross polarization

The summation of the single spectra and the spike removal are subsequently done using a script written in MatLab. The resulting spectrum for T = 6K with cross polarization is displayed in Fig. 12.

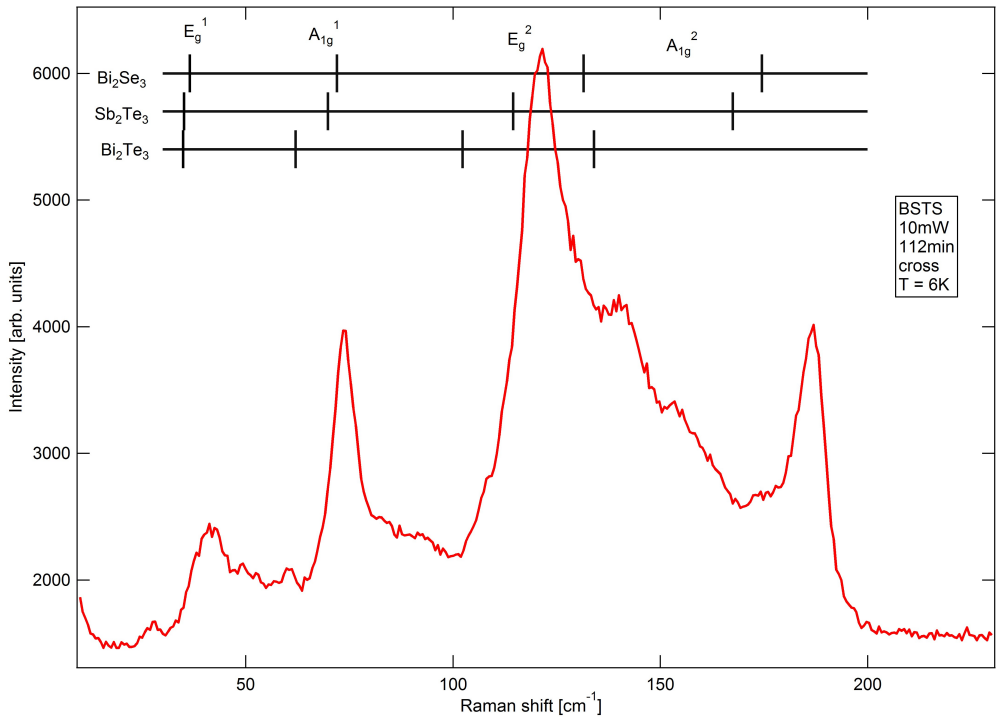

Figure 12: Summed and spike-cleaned cross-polarized Raman spectrum of BSTS measured at T = 6K. For comparison, the Raman shifts of the E_g and A_{1g} modes for Bi_2Te_3, Bi_2Se_3 and Sb_2Te_3 are shown. [18,19,21,22]

A first look at the spectrum suggests that there are four characteristic peaks of considerably high intensity at about 40cm^{-1}, 70cm^{-1}, 120cm^{-1} and 180cm^{-1}. These peaks fit those known to appear for binary compounds consisting of the elements included in BSTS [18,19,21,22]. Following these sources, the four peaks can be identified as A^1_{1g}, E^1_g, A^2_{1g} and E^2_g modes. Of the high intensity peaks, at least the two peaks with the highest Raman shifts appear to be asymmetric. This may hint at additional low intensity modes close to the main peaks. Between the four main peaks, more peaks of lower intensities can be seen. Those peaks can be assumed to originate from the same vibrations as the four main modes, but under participation of different elements. In order to identify the participating elements that lead to the peaks in the spectrum, the Raman shifts can be compared to those known to appear in Bi_2Te_3, Bi_2Se_3 and Sb_2Te_3 binary compounds [18,19,21,22]. The shifts are marked in the spectrum in Fig. 12. The E^1_g, A^1_{1g} and A^2_{1g} modes

of BSTS are all at higher energies than in any of the binary compounds that are used for comparison. This makes it impossible to assign the measured peaks to certain atomic movements in the material. The E_g^2 mode appears at an energy that is higher than in the Bi_2Te_3 and Sb_2Te_3 spectra, but lower than in the Bi_2Se_3 spectrum. So this peak can not be assigned to a certain atomic movement, either. The A_{1g}^2 mode has the biggest deviation from its position in the spectra of the binary compounds. Its appearance at such a high energy suggests that the mode involves movements of Antimony and Selenium atoms, which are the lightest of the four. The peak positions for Sb_2Se_3 can not be used for comparison here, because Sb_2Se_3 has a different crystal structure and does not belong to the R-3m space group but to the Pnma space group (no. 62)[23]. As a result of this, it has different Raman active modes.

The spectrum measured with parallel polarization is shown in Fig. 13.

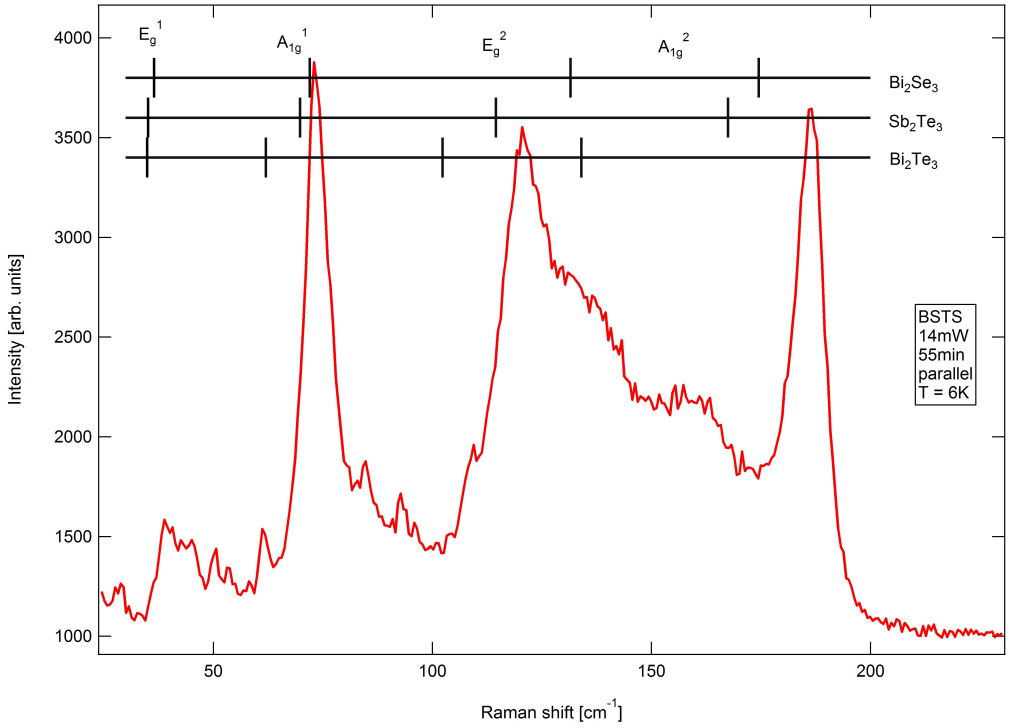

Figure 13: Summed and spike-cleaned parallel polarized spectrum for BSTS at T = 6K. For comparison, the Raman shifts of the E_g and A_{1g} modes for Bi_2Te_3, Bi_2Se_3 and Sb_2Te_3 are shown. [18,19,21,22]

As a result of the shorter exposition time of 55 minutes in comparison to 70 minutes for the cross polarized spectrum, the parallel spectrum clearly shows more noise. This may become a problem when trying to identify the modes, as low intensity modes can disappear in the noise, while strong noise can be misinterpreted as real modes. Generally, the four peaks mentioned in the cross polarized spectrum can be seen here, too. However, the intensities in relation to each other have changed, the A_{1g}^1 mode now giving the strongest signal, while the E_g^2 mode is weakened. Similar to the cross measurement, additional peaks can be suspected especially at 140 cm^{-1} and 150 cm^{-1}. Since the positions of the peaks are in agreement with the position in the cross polarized spectrum, the modes can not be assigned to specific atomic movements, either.

4.2 Temperature-Dependent Development

This section will provide a look at the modes' temperature dependence. The data first has to be normalized for both the overall exposition time and the laser power. The parallel polarized spectra were normalized to 50 minutes and the cross polarized spectra to 70 minutes of total exposure time. The graphs have different backgrounds, so offsets are added to the graphs to level them out. The spectra can be seen in Fig. 14 and Fig. 15

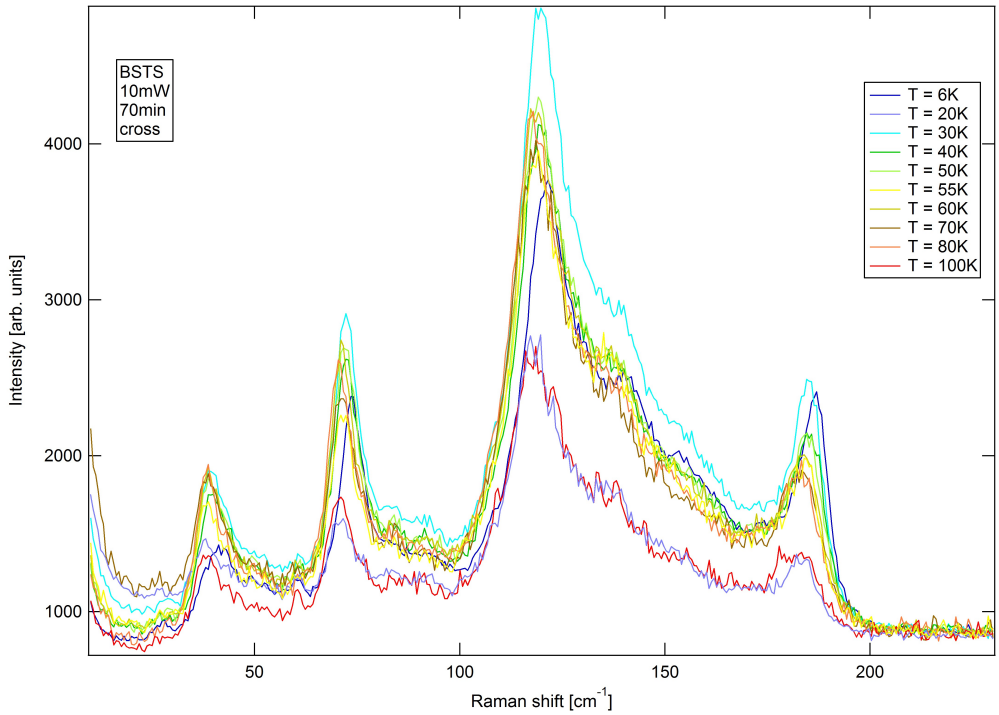

Figure 14: Comparison of the cross polarized Raman spectra of BSTS for different temperatures between 6K and 100K. Offsets have been added to all data except for the T = 20K data in order to equalize the background signal to one level.

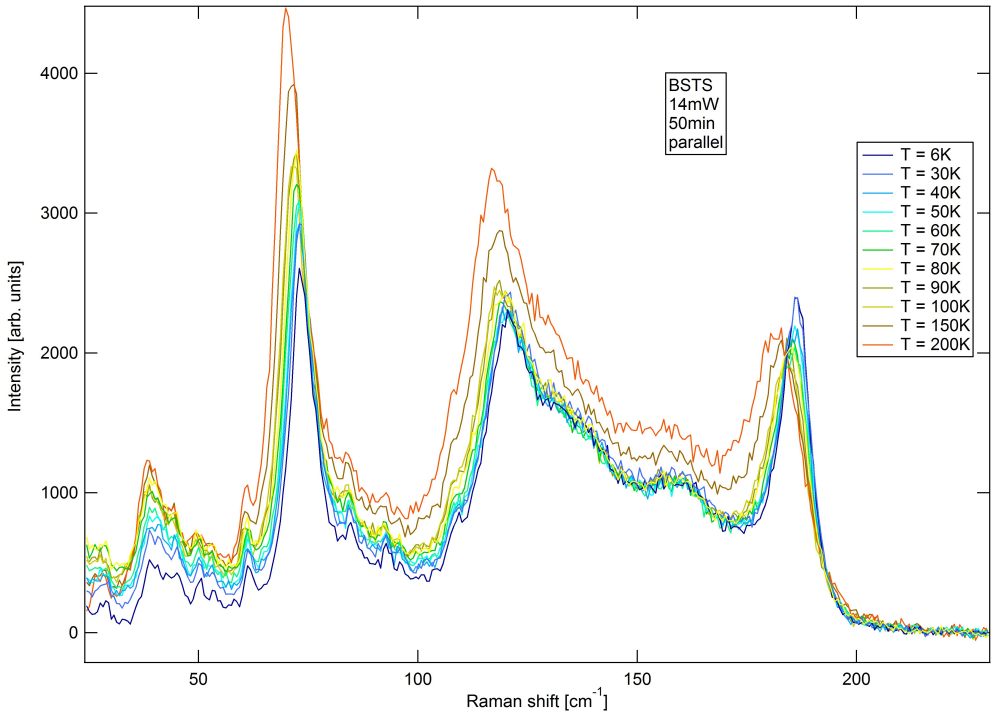

Figure 15: Comparison of the parallel Raman spectra of BSTS for different temperatures between 6K and 200K. Offsets have been added to all data except for the T = 100K data in order to equalize the background signal to one level.

The offsets applied to the graphs are listed in tables 1 and 2 in the appendix.

The first thing to note is that, as already remarked during the measurement, the cross-polarized data for T = 20K have visibly lower intensities than the majority of the other graphs as the laser spot's position on the sample was moved to a spot with lower reflectivity. Unexpectedly, the spectrum obtained for T = 100K shows the same reduced intensities. Contrary to the 20K measurement, which was the very last measurement except for room temperature, the beam position on the sample was not changed for this temperature. Possibly, the spot slightly moves when the temperature is changed, and when setting the temperature to T = 100K it moved to a spot with very low reflectivity. In the parallel polarized measurement, the spectra for T = 150K and T = 200K show higher intensities then at the other temperatures.

It should be noted that there is a general difference between parallel and cross polarized measurement considering the temperature dependency of the background. In the parallel polarized measurement, the background level and therefore the offset that has to be applied to the graphs here is nearly constant for all the temperatures except for 200K. In the cross polarized measurement, it increases approximately linearly with temperature.

To make the different graphs more comparable, the disturbing intensity and background differences are corrected by normalizing the spectra with their integrals. To integrate the spectra, the background is erased by fitting a constant function to the data for wavelengths greater than 210cm^{-1} and subtracting its value from the data. The background intensities can be found in tab. 3 and 4.

I chose the values of 30 cm^{-1} as lower integration limit and 210 cm^{-1} as upper integration limit for the cross polarized data, as these are the wavenumbers where the tails of the peaks with the highest and lowest energy respectively disappear for all temperatures. For the data from the parallel-polarized measurement, 220 cm^{-1} is used as upper integration limit. Trapezoidal integration is used as integration method, as the difference in wavelengths between the points in our measurement is too large for rectangular integration to give sufficiently precise results. The determined values for the integrals can be found in tab. 5 and tab. 6.

Finally, the data are normalized by dividing it through its integral's value. The results for some of the temperatures' data is shown in Fig. 16 and 17.

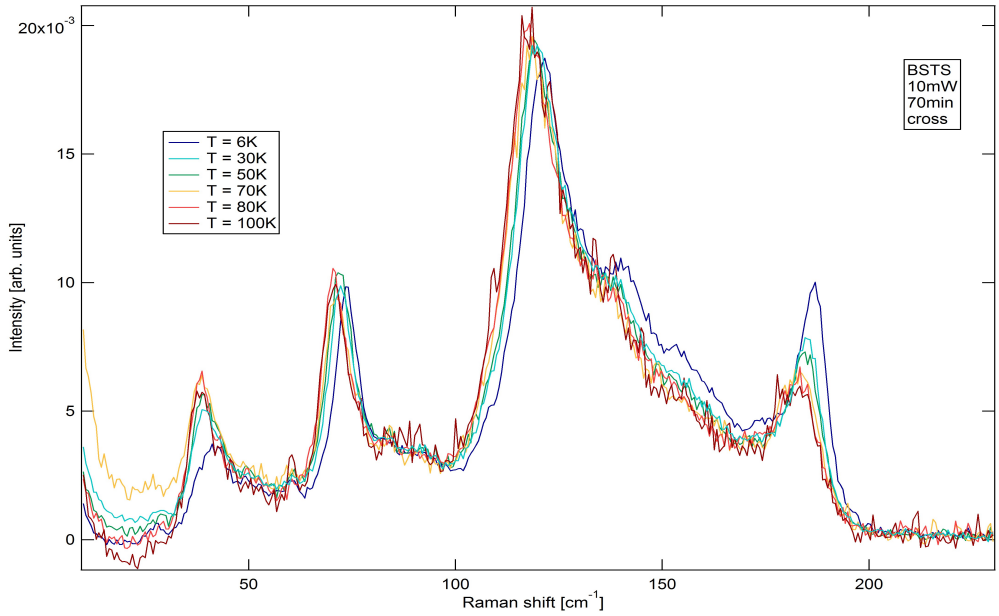

Figure 16: Comparison of the normalized cross polarized Raman spectra of BSTS for different temperatures between 6K and 100K.

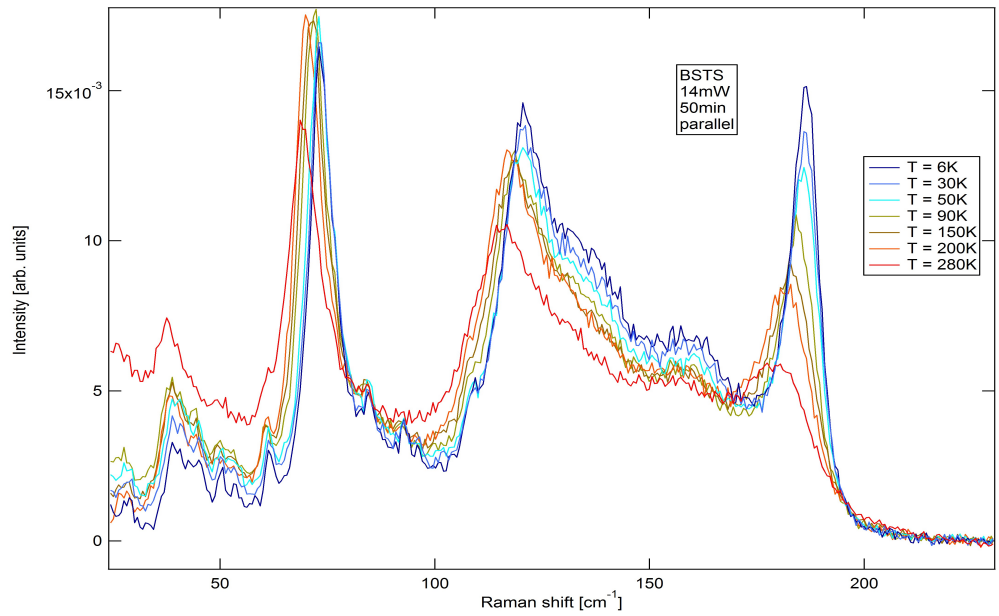

Figure 17: Comparison of the normalized parallel polarized Raman spectra of BSTS for different temperatures between 6K and 280K

For better visibility, only some of the graphs are shown. In this graph, we can qualitatively see the temperature dependent developments for the four main peaks. For all of them, the Raman shift and therefore the mode's energy visibly decreases with temperature. The width of the peak at 180 cm^{-1} seems to increase while for the 30 cm^{-1} it decreases.

In Fig. 18 and Fig. 19, the spectra were shifted along the intensity scale to see the temperature dependence of the modes. This is done by adding a linearly temperature dependent offset to the graphs of Fig. 14 and Fig. 15, except for the high temperature graphs, where the offset is chosen in a way so that they fit the graph. The results are shown in Fig. 18 and Fig. 19.

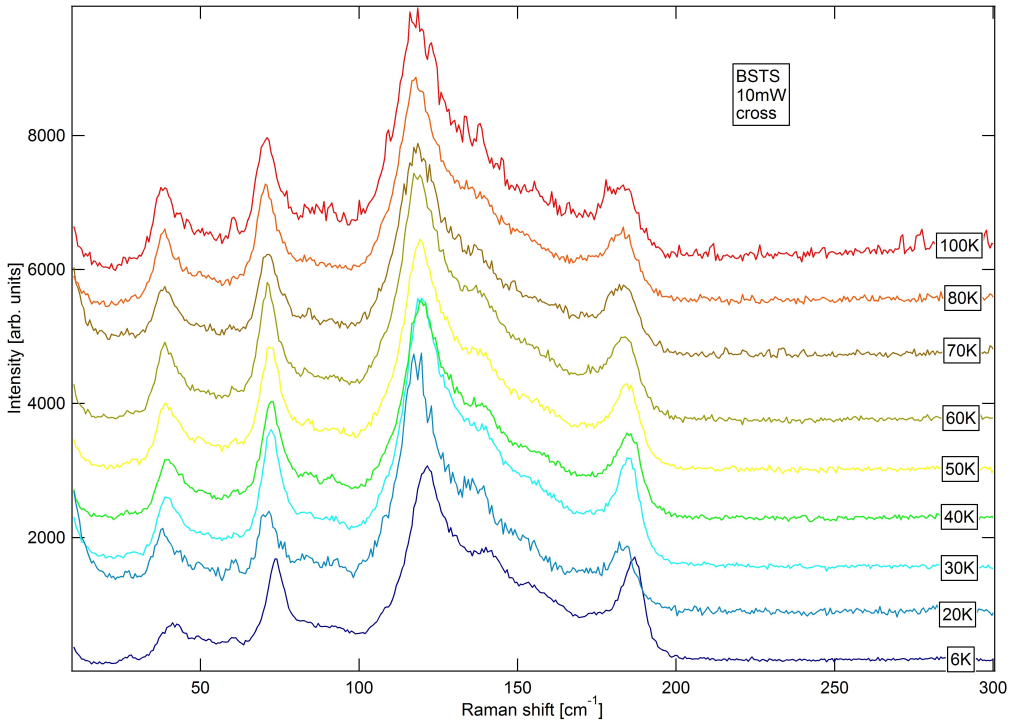

Figure 18: Plot of the cross Raman spectra of BSTS, offsets were added to arrange the graphs above each other.

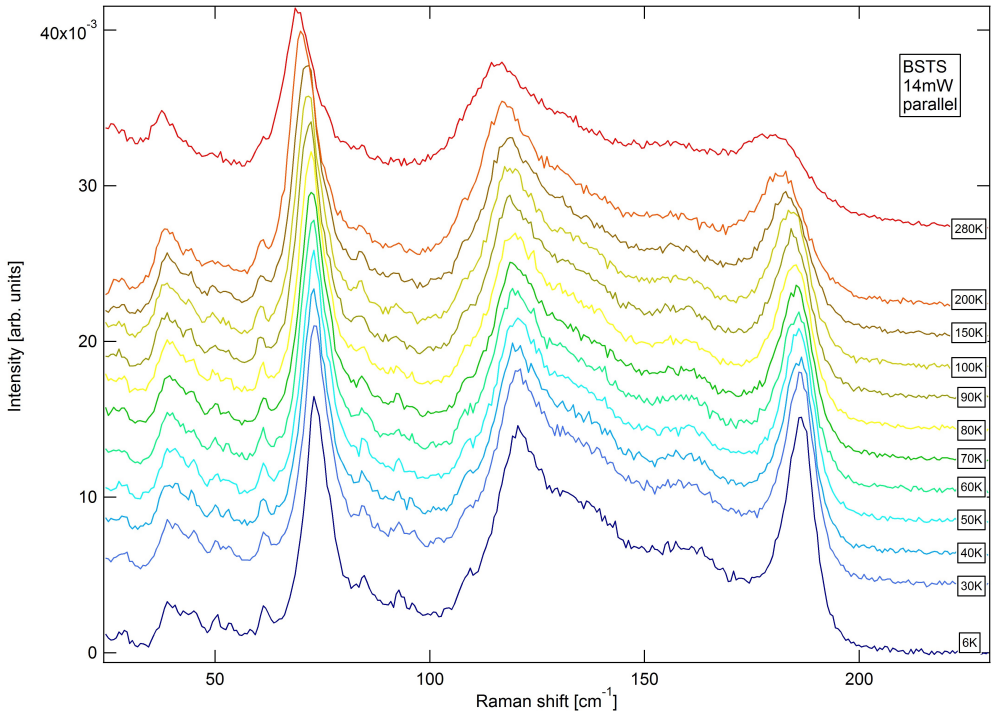

Figure 19: Plot of the parallel Raman spectra of BSTS, offsets were added to arrange the graphs above each other.

The Raman shifts in the 20K cross polarized spectrum and therefore the energies of the modes were observed to be considerably lower than at the temperatures next to it. Unfortunately there was no measurement at T = 20K with parallel polarization, so its not clear if this shift is reappearing there. However, even without having comparable data from the other measurement, it seems reasonable to assume that the shift is not caused by an actual, physical change in the material like a phase transition, but rather is a side effect of the spot change on the sample. From the previous section, it is clear that the modes' energy and therefore the position of the peaks in the spectrum strongly depends on the composition of the material. Of course, Raman measurements on different spots of the material can only be expected to give the same results if the material is homogeneous. The shift of the cross-polarized 20K spectrum suggests that it is not homogeneous. This could for example happen if the Sb or Se doping is locally not exactly as was

assumed. However, with the spot change during the parallel measurement, this did not happen. In that case, no sudden shift was observed, indicating that the composition of the sample was comparable at both spots.

To study the temperature development precisely, it certainly is not sufficient to look qualitatively at the spectra. So in the next part, a multi peak fit will be done for all the graphs. This will give quantitative results for the temperature dependence of all the Raman shifts, widths and intensities. To determine the number of peaks, I did the first fit on the T = 6K spectrum for both polarizations. They are displayed in Fig. 20 and Fig. 21.

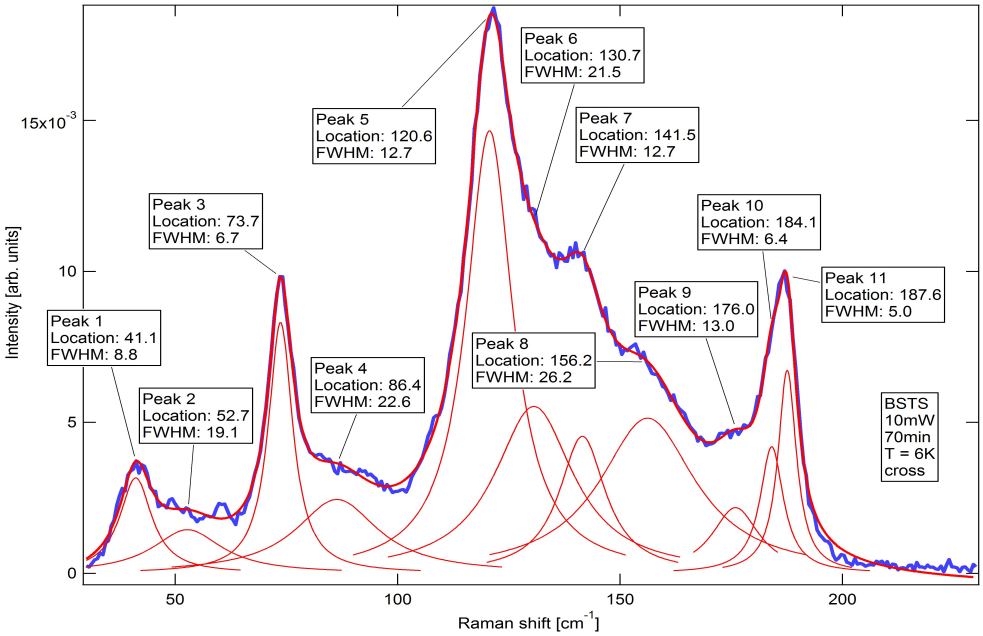

Figure 20: Multipeak fitting results for the T = 6K cross polarized spectrum.

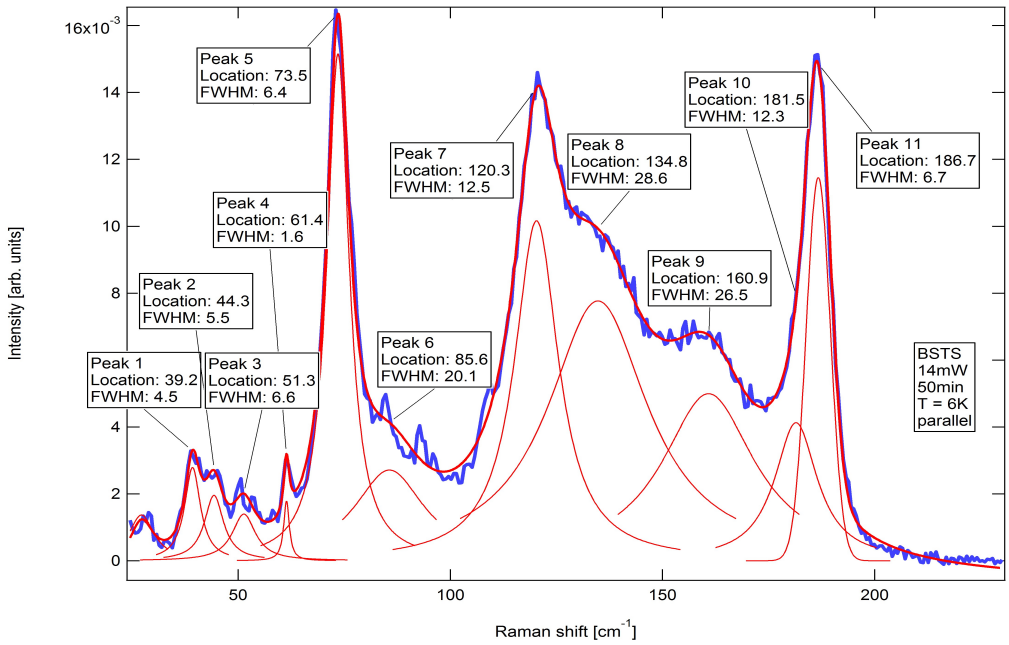

Figure 21: Multipeak fitting results for the T = 6K parallel polarized spectrum.

It should be noted first, that the fits for parallel and cross polarized measurement do not use the same peaks. In fact, only the four main peaks can be fitted similar enough for both polarizations to compare them later. The peaks are all fitted using a Lorentzian line shape. This line shape is used for spectral lines that are affected by natural line broadening and collision line broadening. Generally, in spectroscopy, the peaks can also be affected by Doppler broadening. This is not the case when investigation Raman spectra measured on solids. It is clearly visible that in the parallel spectrum, the equivalent of the cross spectrum's first peak is split in two peaks that have to be treated separately. The mode labeled as *Peak 4* in the parallel spectrum might also exist in the cross spectrum, but since it would hardly be above noise level, it can't be fitted properly there. *Peak 5* is asymmetric in the cross spectrum and so another peak, *Peak 6*, has to be added at its slope to catch the asymmetry. This is not the case in the parallel spectrum, probably because the following peak (Nr. 8 in the parallel spectrum) has a higher intensity here. Special attention should be paid to the peak at 186

cm^{-1}. Since it is asymmetric for both polarizations, two peaks have to be used to get a good fit. For cross polarization, a fit using two Lorentzian peaks gives the best results. For parallel polarisation, this doesn't work at all. Instead, as a second peak, a Gaussian-shaped peak is used here. Near the lower limit of the parallel spectrum, at about 25 cm^{-1}, there might even be another peak. Since it is not completely included in the spectrum and does not appear at all in the cross spectrum because the Rayleigh tail is beginning there, it won't be analysed here. It is included in the parallel spectrum's fit because otherwise the fit for the first real peak wouldn't work as good as it does here. The fits for the other temperatures' spectra are done in the same way as in the respective 6K spectrum.

4.3 Temperature Dependent Analysis of the Modes' Properties

The temperature-dependent Raman shifts are displayed in Fig. 22 and Fig. 23. To determine the error values, the peaks were deliberately shifted from their determined position and fixed there. Then the fit was redone. The shift that has to be applied in order to change the fit so drastically that it doesn't describe the data sufficiently any more is noted as the corresponding error value for each peak.

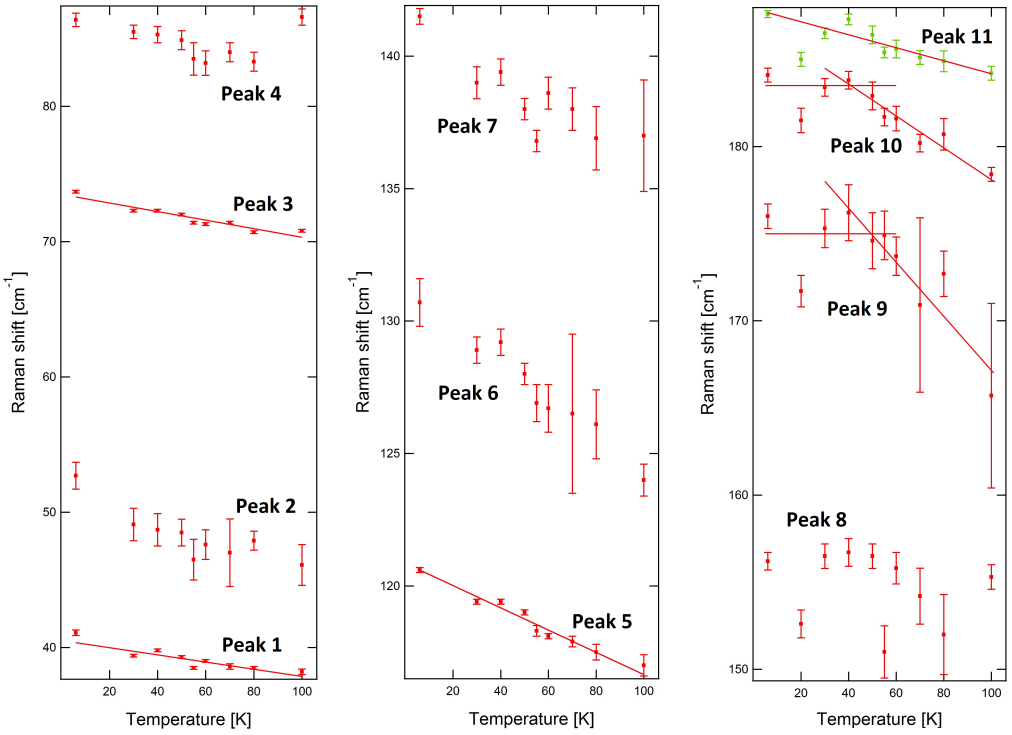

Figure 22: Plot of the temperature-dependent Raman shifts from the cross-polarized measurement

As was already seen in the qualitative comparison of the spectra for different temperatures, the Raman shifts of the data measured at T = 20K are clearly lower than those of the data surrounding it. The data obtained for the other temperatures show a decrease in Raman shift for almost all peaks. Particularly, the four high intensity peaks 1, 3, 5 and 11 decrease linearly with temperature. Using a linear fitting algorithm, the slope of the Raman shift with regard to temperature was determined for these four modes. The data for T = 20K was not included in the fits. The fits are also displayed in Fig. 22 and the slopes can be found in tab. 7 in the appendix. Over the considered temperature range from 6K to 100K, peaks 1 and 3 both shift by 2.9 cm^{-1}, peak 5 shifts by 3.6 cm^{-1} and peak 11 shifts by 3.4 cm^{-1}. There are also two peaks (peaks 10 and 11) that show an approximately constant Raman shift for temperatures below 50K, but a linearly decreasing shift for temperatures higher than 50K.

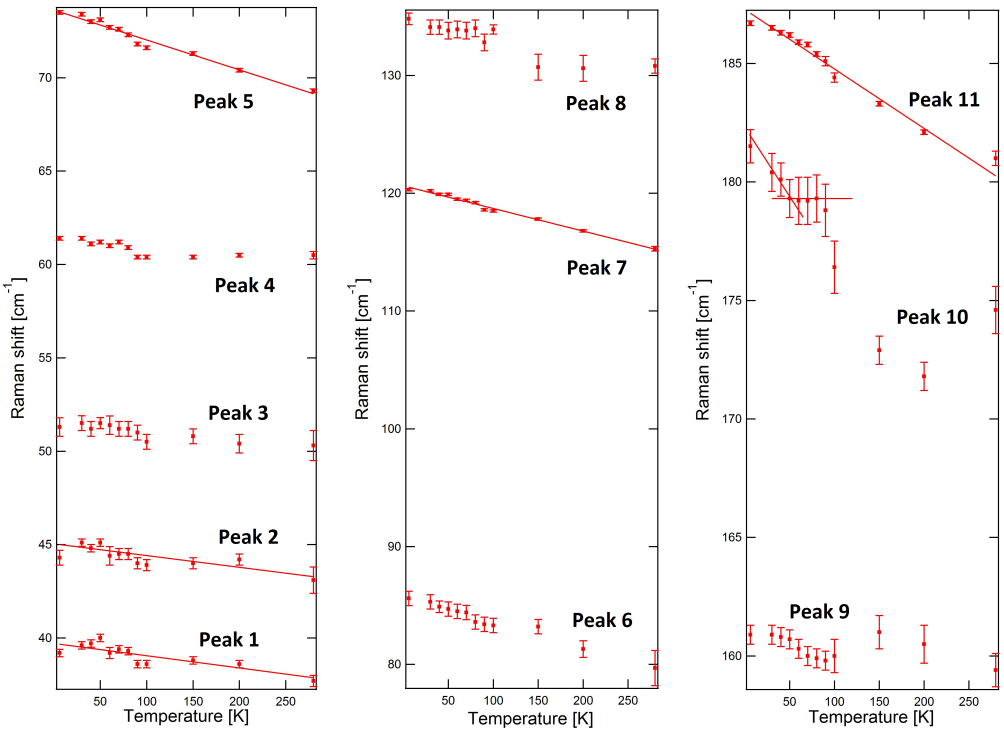

Figure 23: Plot of the temperature-dependent Raman shifts from the parallel polarized measurement

The Raman shifts for the parallel-polarized measurement are also increasing with decreasing temperature. Noticeable deviations from the linear behaviour can be seen on peaks 9 and 10. While peak 9 shifts to higher wavenumbers for temperatures above 100K, peak 10 shows the same change in behaviour at about T = 50K as it does in the cross polarized measurement, but then rapidly decreases starting at 100K. However, peak 10 is only a supporting peak created to consider the asymmetry of peak 11 and so it is difficult to fit it consistently above the whole temperature range. The four most distinct peaks 1, 2, 5 and 11 decrease linearly. As was done for the cross-polarized measurement, the temperature-dependent slopes of the Raman shifts of these peaks are determined using a linear fit, which can be seen in the diagram. The results are stated in tab. 8 in the appendix. Over the measured temperature range, peak 1 shifts by 1.5 cm^{-1}, peak 2 shifts by 1.3 cm^{-1}, peak 5 shifts by 4.2 cm^{-1} and peak 11 shifts by 5.7 cm^{-1}. What

is most important for this research is that for almost all peaks, there is no special behaviour like a minimum in Raman shift at T = 50K. Instead, the modes behave fairly even with regard to temperature. The only exception to this might be Peaks 10, which shows a change at T ≈ 50K.

To complete the analysis of the spectra, we will now have a look at the temperature-dependence of the width and intensity of the four main peaks. The widths are plotted in Fig. 24 and Fig. 25.

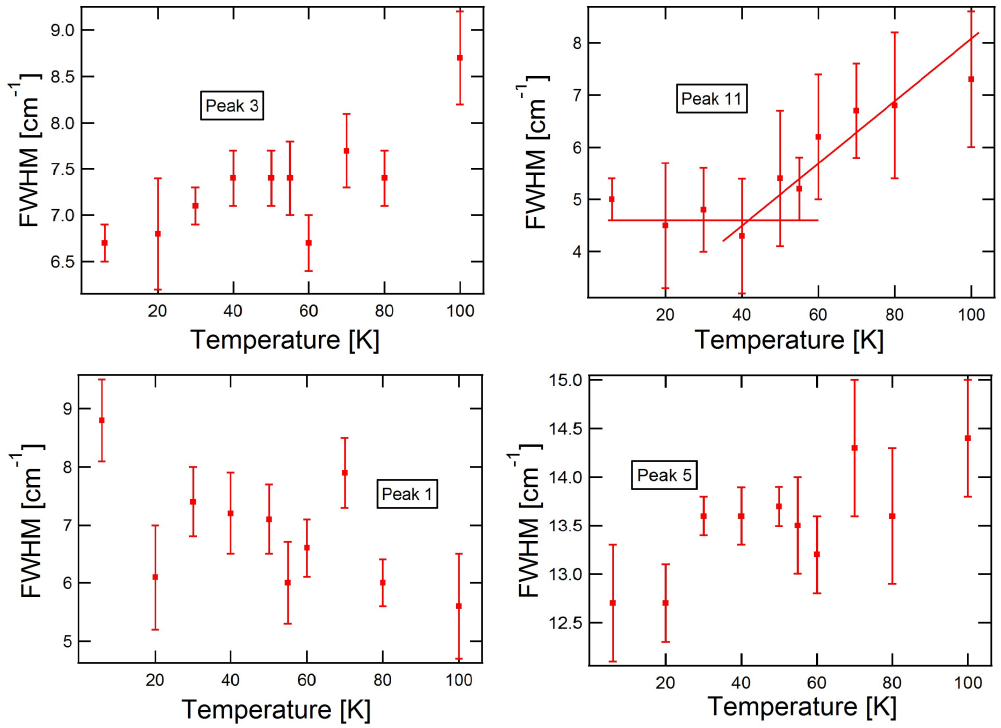

Figure 24: Plot of the temperature-dependent Full Width at Half-Maximum (FWHM) from the cross-polarized measurement

The width of peak 1 decreases by about 3.2 cm^{-1} in total, while the width of the three other peaks increase by 2 cm^{-1} (peak 3), 1.7 cm^{-1} (peak 5) and 2.3 cm^{-1} (peak 11), respectively, over the temperature range from 6K to 100K. The data for peak 11 shows a switch from constant to linearly increasing behaviour to the change in Raman shifts for peak 9 and 10 seen above.

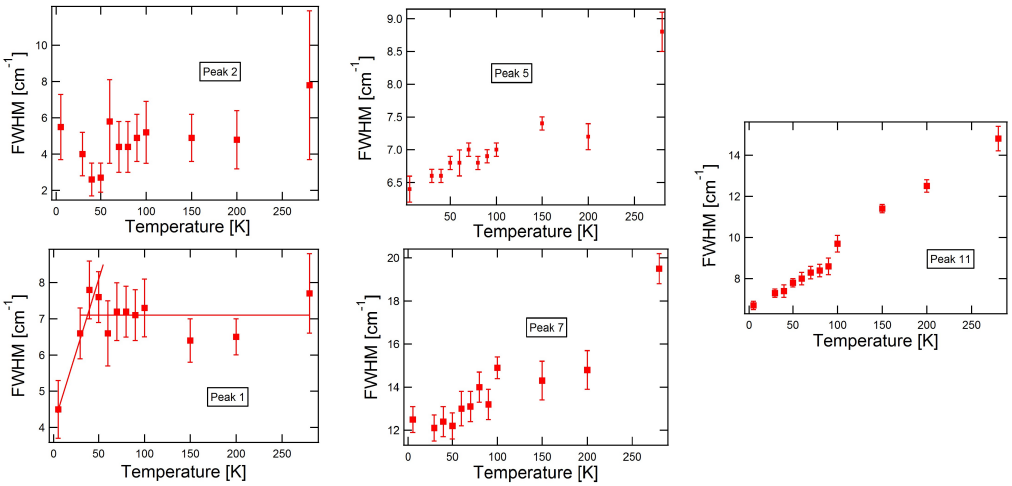

Figure 25: Plot of the temperature-dependent Full Width at Half-Maximum (FWHM) from the parallel-polarized measurement

In the parallel-polarized spectrum, peaks 5, 7 and 11 have an increasing FWHM with increasing temperature. Peak 1 shows an increasing width for temperatures below 40K and a constant width for higher temperatures. For temperatures below 40K, Peak 2 shows opposingly has a decreasing width. Since peak 1 and 2 are very close in the spectrum, the strong temperature dependence of the width might also be caused by fitting problems or the spectral resolution limit. Over the range from 6K to room temperature, peak 1 increases by 2.2 cm^{-1}, peak 2 increases by 2.3 cm^{-1}, peak 5 increases by 2.4 cm^{-1}, peak 7 increases by 7, although the value for room temperature seems to be a little too high to fit the other values, cm^{-1} and peak 11 increases by 8.1 cm^{-1}.

The intensities are plotted with regard to temperature in Fig. 26 and Fig. 27.

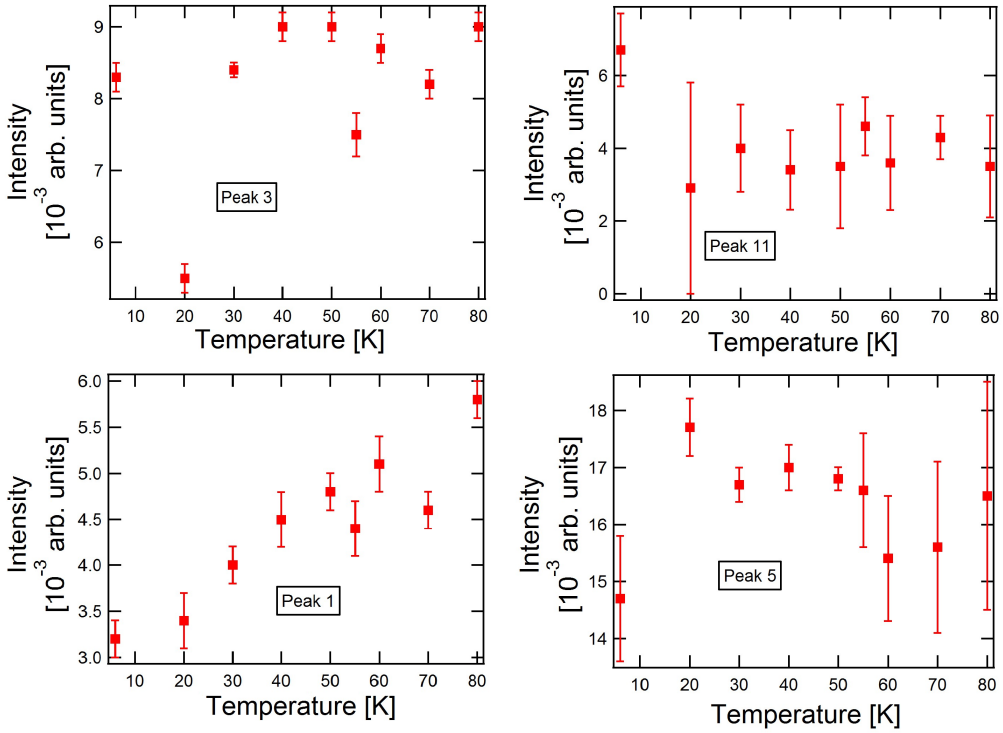

Figure 26: Plot of the temperature-dependent intensity from the cross-polarized measurement

It is notable that the decrease in intensity of peak 11 is not as strong as it was expected after seeing the spectrum. This is because of the additional peak 10 which supports peak 11. Since the two peaks are so close to each other, they can not be fitted independently, and so the intensity decrease is probably partly caught by peak 10. Peak 1 increases by 2.6 $\cdot 10^{-3}$ a.u., Peak 3 increases by 0.7 $\cdot 10^{-3}$ a.u., Peak 5 increases by 1.8 $\cdot 10^{-3}$ a.u. and Peak 11 decreases by 3.2 $\cdot 10^{-3}$ a.u. . No striking changes at T $\approx$ 50K can be seen here.

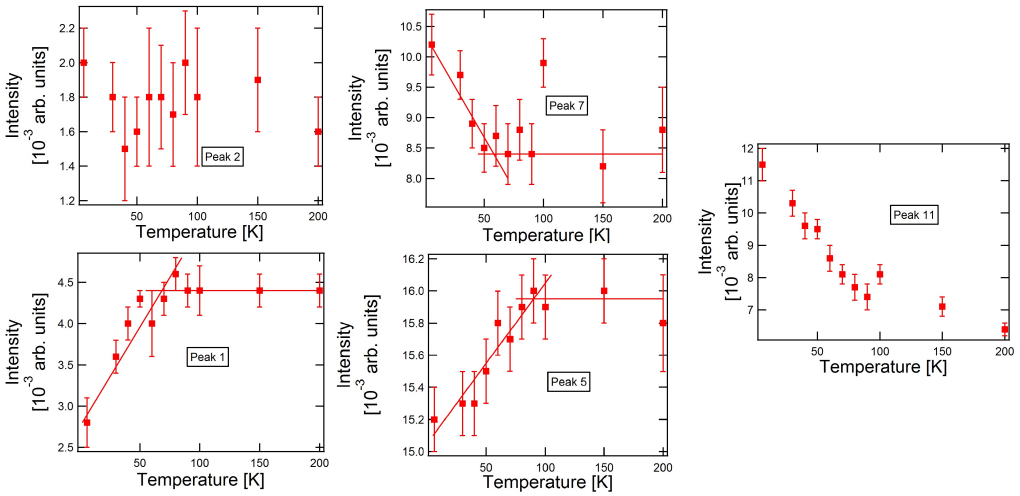

Figure 27: Plot of the temperature-dependent intensity from the parallel-polarized measurement

For the parallel-polarized measurement, the qualitative prediction is closer to the actual result. Peak 11 decreases by 8.1 $\cdot 10^{-3}$ a.u., which fits Fig. 15. Peak 1 increases by 2.4 $\cdot 10^{-3}$ a.u., peak 2 decreases by only 0.5 $\cdot 10^{-3}$ a.u., peak 5 decreases by 4.4 $\cdot 10^{-3}$ a.u. and peak 7 decreases by 2.4 $\cdot 10^{-3}$ a.u., all those results fit the expectation from the spectrum. Contrary to the intensities from the cross polarized measurement, 27 shows that the temperature dependence might change from linearly increasing to constant behaviour for peaks 1 and 5 and from linearly decreasing to constant behaviour for peak 7. The highest energy mode is fitted by two peaks. Since the two peak fits will definitely influence each other, the peak parameters for this mode are difficult to analyse. To get useful information about this mode, other parameters have to be used. In this case, the right slope of the peak will be analysed with regard to temperature. To get those slopes, linear fits are done at the right side of the peak. The temperature dependent results can be found in Fig. 28 and Fig. 29.

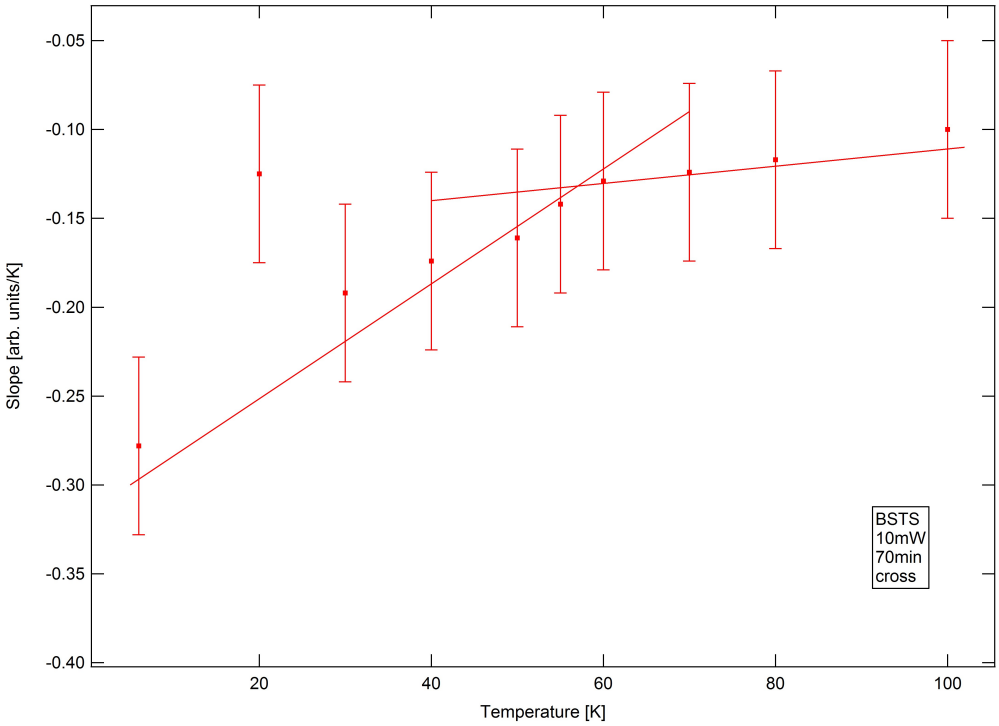

Figure 28: Temperature dependence of the highest energy peak's right slope from the cross polarized measurement

Here again, the value for 20K doesn't fit. So apparently, the oddity is not limited to the peaks' positions. Excluding the T = 20K value, Fig. 28 shows a change in the temperature dependence of the slope around 60K. At both higher and lower temperatures, the slope increases approximately linear with temperature. However, the increase is visibly stronger for temperatures below 60K. This could be another hint at a change within the material at around 50K. It is also possible that this change in the graph is not material induced, but rather caused by the resolution limit of the detector. As can be seen in the graphs for the temperature dependent Raman shifts, the two peaks get closer for lower temperatures. If the resolution limit is reached, this could lead to the observed decrease in the slope of the peak.

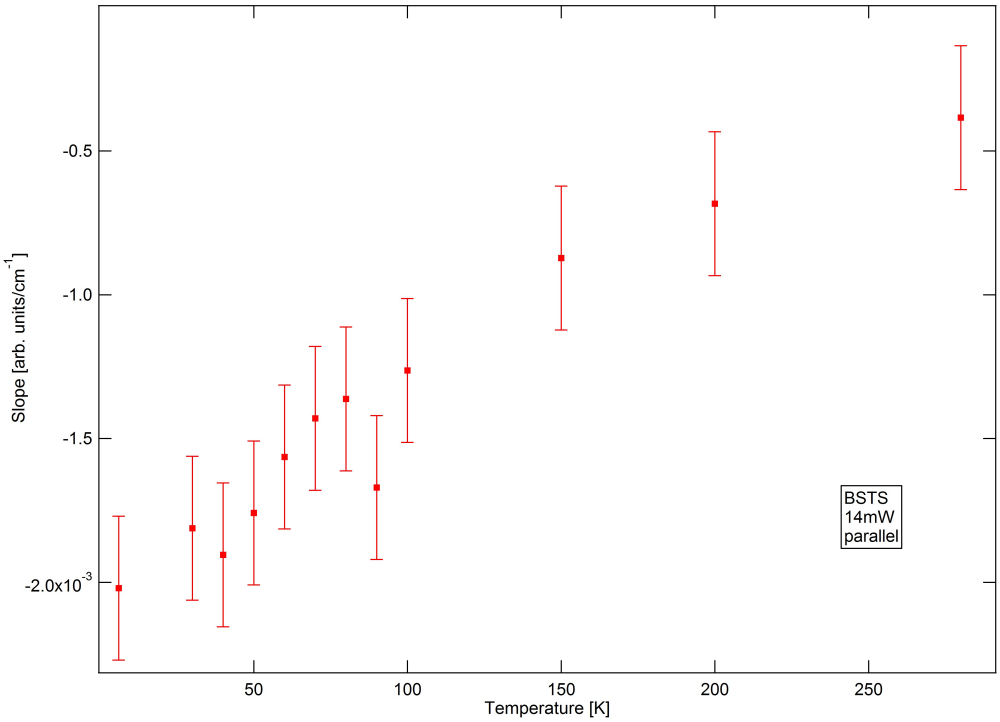

Figure 29: Temperature dependence of the highest energy peak's right slope from the cross polarized measurement

Contrary to the observations on the slopes of the high energy peak in the cross polarized spectrum, the corresponding graph for the parallel polarized measurement does not show a change in temperature dependence behaviour

5 Conclusions

The Raman spectrum for $BiSbTeSe_2$ was successfully measured at different temperatures between 6K and 280K using the Macro optical Raman setup.

Like Bi_2Te_3, Bi_2Se_3 and Sb_2Te_3, BSTS has four main vibrational modes that can be identified as the A^1_{1g}, E^1_g, A^2_{1g} and E^2_g modes that are known to exist for these compounds. However, the positions of these four modes do not coincide with those that can be obtained from the literature for the binary compounds. Especially, the peak with the highest energy shows a Raman shift that is larger than any Raman shift in the three compounds. In addition to these four peaks, there are also some peaks with lower intensities. These peaks should originate from the same modes under participation of different atoms. Same as for the high intensity peaks, an exact assignment of the peaks to a binary compound can not be done satisfactory.

The analysis of the temperature dependence of the main Raman active modes observed in BSTS showed that for all four modes, the Raman shift decreases linearly with temperature. The temperature development of the two other discusses parameters, the width and the intensity, is not as stable as the Raman shifts' development, but mostly also follows linear patterns. In the parameter analysis, some indications for non-trivial behaviour at T = 50K could be found. For some modes, the temperature dependence of either the Raman shift, the width or the intensity changes from a constant to a linear dependence or the other way around. However, these changes do not appear consistently for the individual peaks. Instead, the peaks mostly show this behaviour in only one of the analysed parameters or none at all. Additionally, some of these changes might be attributed to measurement and analysis problems that occur when two of the modes are very close in the spectrum.

In total, there are only small indications for a significant change in the material at around T = 50K. Most of the Raman data suggests that at least the material properties that influence the Raman spectrum have a monotonic temperature dependence.

6 Acknowledgements

Although this bachelor project could not doubtlessly verify the unusual temperature behaviour that was suggested by previous measurements, the measurement and analysis in general worked without serious problems. In any case, it taught me a lot of things about Raman spectroscopy, data analysis and scientific work in general.

For all this, I firstly and mainly want to thank Raphael German. For initially installing the Macro setup with me and helping throughout the measurement, for providing me with the necessary skills (and programs) to analyse the data, for proofreading the thesis and especially for answering the great many questions I had while measuring and while writing it. I suppose it can't have been easy to calmly explain for the fifth or sixth time which outlet from the helium distribution pipes has to be closed or opened when and why.

Secondly, I want to thank Prof. Dr. ir. Paul H. M. van Loosdrecht for his guidance during this thesis, for multiply discussions about the data, its analysis and the meaning of the results, and of course for initially suggesting the topic and introducing me to it. I am very glad to have chosen this topic for my bachelor thesis.

Not only did this choice allow me to research an interesting topic in solid state physics, but it also introduced me to the OCMS work group and its members. I want to thank the whole work group for providing a very nice time in the last months. Special thanks goes to Bernhard Zimmer, who wrote the MatLab script that I used to analyse the Raman data.

7 References

[1] M. König, S. Wiedmann, C. Brüne, A. Roth, H. Buhmann, L.W. Molenkamp, X.-L. Qi, S.-C. Zhang, *Quantum Spin Hall Insulator State in HgTe Quantum Wells* (2007)

[2] N. Borgwardt, J. Lux, I. Vergara, Z. Wang, A.A. Taskin, K. Segawa, P.H.M. van Loosdrecht, Y. Ando, A. Rosch, M. Grüninger, *Revealing Puddles of Electrons and Holes in compensated Topological Insulators* (2015, unpublished)

[3] L. Fu, C.L. Kane, E.J. Mele, *Topological Insulators in three Dimensions*, Phys. Rev. Lett. 98, 106803 (2007)

[4] J.E. Moore, L. Balents, *Topological Invariants of time-reversal-invariant Band Structures*, Phys. Rev. B 75, 121306(R) (2007)

[5] S.-Q. Shen, *Topological Insulators: Dirac Equation in Condensed Matters* (2012), Springer Series in Solid-State Sciences 174, Springer-Verlag Berlin Heidelberg, p. 5-7

[6] A.M. Abou el Soud, B.S. Farag, I.S. Ahmed Farag, S.A. Gad, H.A. Zayed, *Crystal Structure and optical Properties of quaternary Systems of Bi-Sb-Te-Se* (2007)

[7] C.L. Kane, *Topological Band Theory and the $\mathbb{Z}_2$ Invariant* (2013), in M. Franz, L. Molenkamp, ed., *Comtemporary Concepts of Condensed Matter Science, Volume 6: Topological Insulators*, Elsevier, Oxford, p. 3-34.

[8] H. He, J. Wang, *Weak Antilocalization Effect, Quantum Oscillation, and Superconducting Proximity Effect in 3D Topological Insulators* (2015), in F. Ortmann, S. Roche, S.O. Valenzuela, *Topological Insulators: Fundamentals and Perspectives*, Wiley-VCH, Weinheim, p. 331

[9] X. Chen, Z.X. Liu, X.-G. Wen, *2D symmetry protected topological orders and their protected gapless edge excitations*, Phys. Rev. B84, 235141 (2011)

[10] Y. Ando, *Topological Insulator Materials* (2013), J. Phys. Soc. Jpn. 82, 102001

[11] C.L. Kane, E.J. Mele, *A new Spin on the Insulating State* (2006), Science 314, Nr. 5806

[12] C.V. Raman, K.S. Krishnan, Nature 121-501 (1928)

[13] E.O. Potma, S. Mukamel, *Theory of Coherent Raman Scattering* (2013), in J.-X. Cheng, X. Sunney Xie, ed., *Coherent Raman Scattering Microscopy*, CRC Press/Taylor & Francis Group, p. 10-11
[14] J.M. Hollas, *Modern Spectroscopy*, John Wiley & Sons, Hoboken, NJ (2004), p. 166-172
[15] R. Merlin, A. Pinczuk, W.H. Weber, *Overview of Phonon Raman Scattering in Solids* (2000), in R. Merlin, W.H. Weber, ed., *Raman Scattering in Materials Science*, Springer Series in Materials Science, p. 7-26
[16] Horiba Jobin Yvon T64000 User Manual
[17] K.M.F. Shahil, M.Z. Hossain, V. Goyal, A.A. Balandin, *Micro-Raman Spectroscopy of Mechanically Exfoliated Few-Quintuple Layers of Bi_2Se_3, Bi_2Se_3 and Sb_2Te_3 materials* (2012)
[18] W. Richter, H. Köhler, C. Becker, Phys. Stat. Sol. (b) 84, 619 (1977)
[19] Bilbao Crystallographic Server
[20] J. Zhang et al., *Raman Spectroscopy of Few-Quintuple Layer Topological Insulator Bi_2Se_3 Nanoplatelets*
[21] A. Soni, Z. Yanyuan, Y. Ligen, M. Khor Khiam Aik, M.S. Dresselhaus, Q. Xiong, *Enhanced Thermoelectric Properties of Solution Grown $Bi_2Te_{3-x}Se_x$ Nanoplatelet Composites*
[22] W. Kullmann, J. Geurts, W. Richter, N. Lehner, H. Rauh, U. Steigenberger, G. Eichhorn, R. Geick, Phys. Stat. Sol. (b) 125, 131 (1984)
[23] G.P. Voutsas, A.G. Papazoglu, P.J. Rentzeperis, D. Siapkas, *The crystal structure of antimony selenide, Sb_2Se_3*, Zeitschrift für Kristallographie 171, 1985, S. 261-268

8 Appendix

T [K]	6	20	30	40	50	55	60	70	80	100
Offset [a.u.]	-100	0	-200	-260	-350	-310	-400	-560	-760	-500

Table 1: Overview of offsets applied to the graphs in Fig. 14.

T [K]	6	30	40	50	60	70	80	90	100	150	200	280
Offset [a.u.]	-50	-90	-60	-60	-60	-50	-60	-20	0	-70	-720	-930

Table 2: Overview of offsets applied to the graphs in Fig. 15.

T [K]	6	20	30	40	50	55	60	70	80	100
Background [a.u.]	945	845	1045	1105	1195	1155	1245	1405	1605	1345

Table 3: Background data determined for the cross polarized measurements' data

T [K]	6	30	40	50	60	70	80	90	100	150	200	280
Background [a.u.]	920	960	930	930	930	920	930	890	870	940	1610	800

Table 4: Background data determined for the parallel polarized measurements' data

T [K]	6	20	30	40	50
Integral	156200	92361	209393	168484	177857
T [K]	55	60	70	80	100
Integral	156838	176005	162470	167647	89644

Table 5: Integral values for the cross polarized measurements' data

T [K]	6	30	40	50	60	70
Integral	158152	175936	172305	176252	177495	186627
T [K]	80	90	100	150	200	280
Integral	193934	193812	192575	226300	265857	441841

Table 6: Integral values for the parallel polarized measurements' data

Peak Nr.	1	3	5	11
Slope $[\frac{m^{-1}}{K}]$	-2.7 ± -0.2	3.2 ± 0.1	-4.2 ± 0.2	-3.7 ± 0.4

Table 7: Slopes for the Raman shift with regard to temperature for the high-intensity peaks from the cross-polarized measurement

Peak Nr.	1	2	5	7	11
Slope $[\frac{m^{-1}}{K}]$	-0.65 ± 0.09	-0.63 ± 0.1	-1.6 ± 0.04	-1.92 ± 0.05	-2.5 ± 0.05

Table 8: Slopes for the Raman shift with regard to temperature for the high-intensity peaks from the parallel-polarized measurement

List of Figures

Hiermit versichere ich an Eides statt, dass ich die vorliegende Arbeit selbstständig und ohne die Benutzung anderer als der angegebenen Hilfsmittel angefertigt habe. Alle Stellen, die wörtlich oder sinngemäß aus veröffentlichten und nicht veröffentlichten Schriften entnommen wurden, sind als solche kenntlich gemacht. Die Arbeit ist in gleicher oder ähnlicher Form oder auszugsweise im Rahmen einer anderen Prüfung noch nicht vorgelegt worden. Ich versichere, dass die eingereichte elektronische Fassung der eingereichten Druckfassung vollständig entspricht.